

Appendix A: Studies of Numerical Diffusion and Numerical Input Parameters in IFCI

Because IFCI uses a donor-cell differencing technique to model the transport of the three fields, there is some concern about the effect of numerical diffusion on the calculation. In particular, initial IFCI calculations of the MAGICO-701 and MIXA-6 experiments predicted melt transit times from the top of the water to the bottom of the water that were shorter than those actually observed. To determine if this might be caused by numerical diffusion, a series of simplified problems were created.

The simplest configuration that can be compared to a simple calculation is that of a single solid particle dropping through water. This configuration is the basis of this study. The water region for each of the three experiments (MAGICO-701, MIXA-6, KROTOS-26) was coarsely meshed. The top node of each of these three meshes contained an initial “melt” concentration of 1 volume%. The temperatures of the water and the “melt” were set to 373 K, so that no boiling would take place.

Figure 18 shows the calculated MIXA-6 melt concentration for the coarse mesh at 0, 0.14, and 0.24 seconds. In the initial profile, the “melt” has a concentration of 0.01 and occupies one node

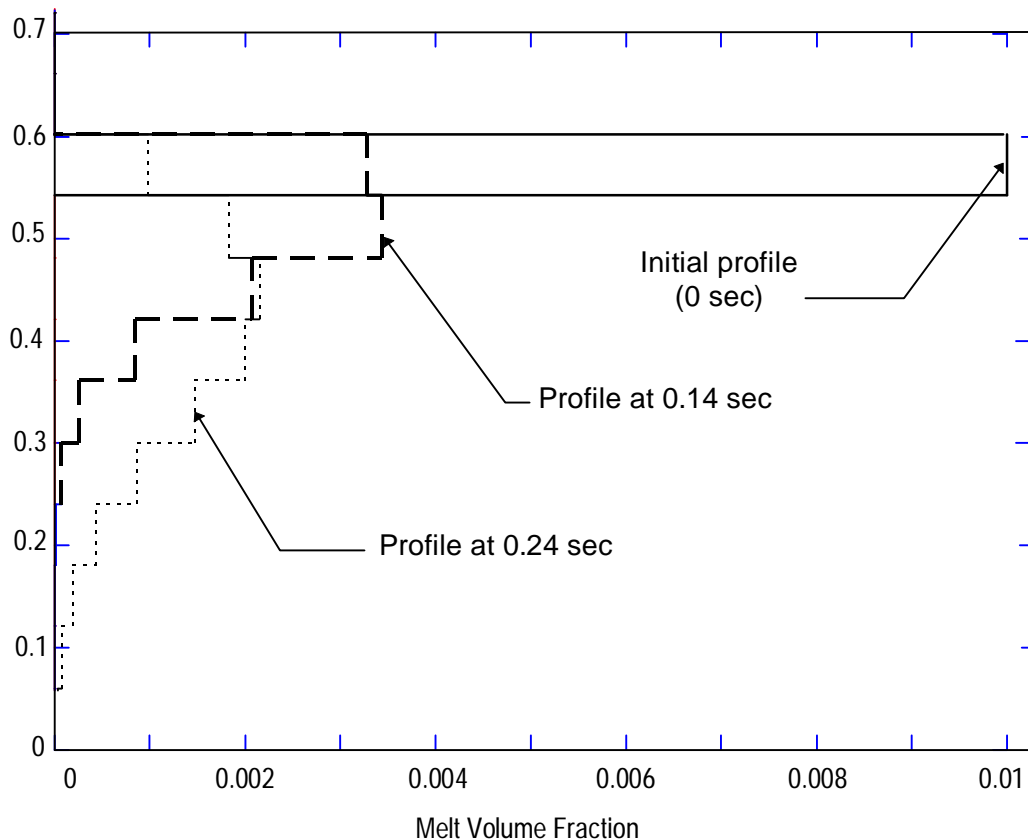


Figure 18 MIXA-6 Melt Concentration Profiles Calculated by Coarse Mesh (10 nodes in the water) at 0.00, 0.14, and 0.24 sec

that extends from 0.54 m to 0.60 m. As time progresses, the width of the “melt” zone broadens and the maximum concentration decreases. In the absence of numerical diffusion, this profile would remain intact, maintaining both the original concentration and a width of 0.06 m.

The only user-controllable way to decrease numerical diffusion in IFCI is to refine the mesh. Figure 19 shows the location of the leading edge of the “melt” front as a function of time for four different meshes. For all meshes, the leading edge is initially located 0.06 m under the top surface of the water. The predicted rate at which the front progresses varies between meshes. Finer meshes decrease the numerical diffusion and the “melt” front takes longer to reach the bottom (at 0.6 m).

Based on the drag coefficients used in IFCI, the melt front should take 0.56 seconds to reach the bottom of the water. This is indicated by a vertical line on the graph. The first three meshes (10, 40, and 80 nodes) display the expected progression toward the “correct” arrival time of 0.56 seconds. The fourth mesh (160 nodes), however, predicts an arrival time of about 0.6 seconds. This unexpected result is an artifact of the multi-field solution technique used in IFCI and is sensitive to a user input value denoted "AL10", which is a threshold volume fraction. The use of AL10 and the symptoms of this sensitivity are described in greater detail next.

Over the course of the calculation, not all fields (water, vapor, “melt”) are present in all cells. This situation can produce singular matrices which halt the calculation. IFCI corrects this

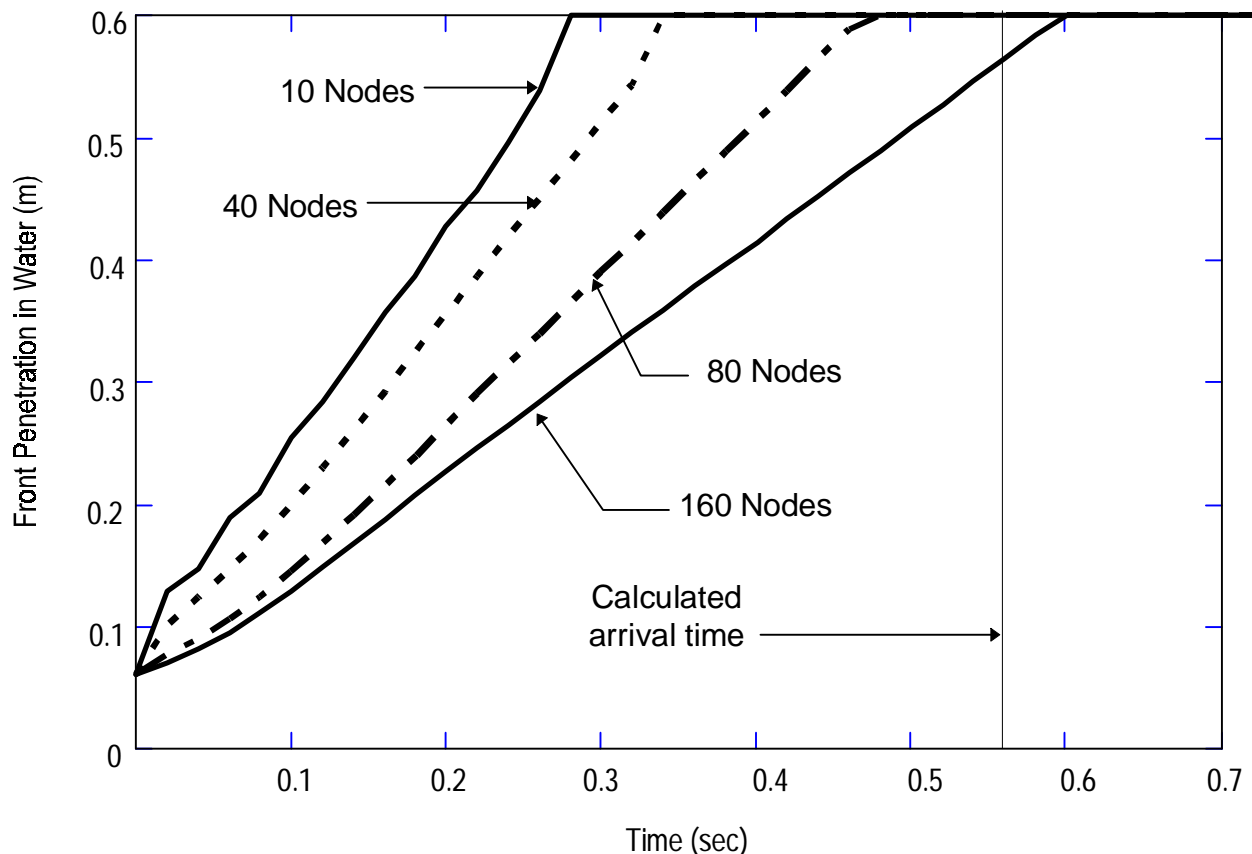


Figure 19 Effect of Mesh Refinement in MIXA-6 on Numerical Diffusion

situation by checking for the presence of a threshold amount of each field in each cell. If the volume fraction of a field in a particular cell is less than the threshold value, that field is excluded in the calculation of the cell variables. Also, convection of the field out of the cell is restricted until the volume fraction of that field exceeds the threshold value.

The threshold volume fraction is specified by the user in the input deck and has the input name of AL10 (p. 33 of reference 16). If this value is too large, the numerical scheme artificially inhibits the convection of the melt. Figure 20 illustrates this problem by showing the "melt" concentration previously presented for the coarse mesh at 0, 0.14, and 0.24 seconds (Figure 18) as calculated by the finest mesh (160 nodes in the water). The problem is seen by comparing the shapes of the profiles at 0.14 and 0.24 seconds. The shape of the concentration profile at 0.14 seconds is reasonable and appears unaffected by the choice of AL10. In addition, one can see that the numerical diffusion is significantly less than that observed in the coarse mesh (compare with Figure 18). However, the concentration profile at 0.24 seconds has been affected by the value of AL10. The leading edge of the profile is much steeper than an unaffected profile, and the peak is characterized by a sharp point. Furthermore, as pointed out earlier, the particle velocities calculated by IFCI for this case are less than what they should be, based upon the drag coefficients used in the code.

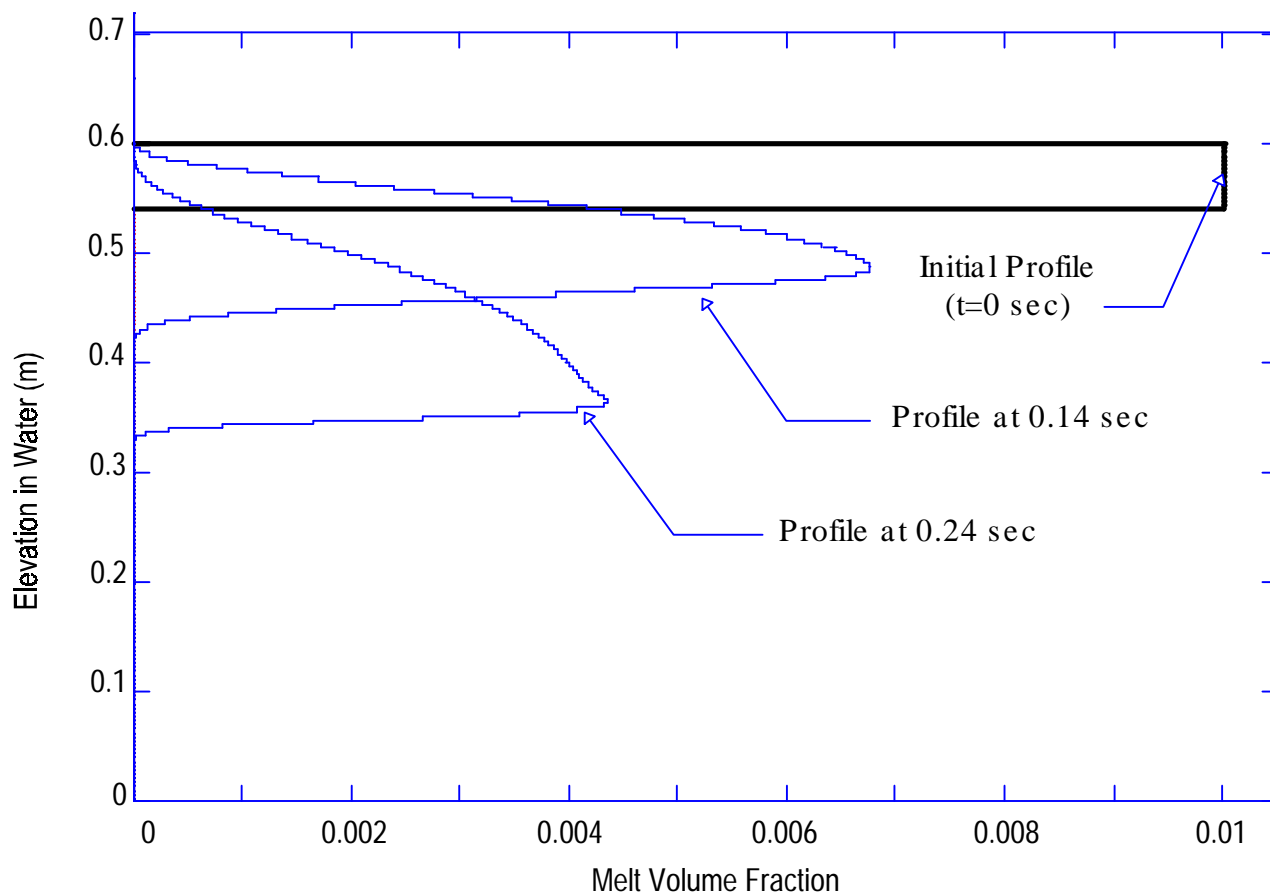


Figure 20 "Melt" Concentration Profiles Calculated by the Finest Mesh (160 nodes in the water) at 0.00, 0.14, and 0.24 sec

Multiple runs in which the value of AL10 was varied prove that this anomaly is clearly attributable to the selection of this input variable. The computer runs made for this analysis used a value of 10^{-16} for AL10. If a larger value is chosen, the numerical retardation of the “melt” will occur in coarser meshes. If a smaller value is chosen, the numerical stability of the run can be threatened.

The appearance of this particular numerical anomaly appears to be problem-dependent. Figure 21 shows the effect of mesh refinement on numerical diffusion for the MAGICO-701 calculation. All of the mesh resolutions examined appear free of the numerical retardation associated with AL10. Progressive refinement of the mesh causes the calculated front arrival time to approach the value of 0.38 seconds, calculated directly from the drag coefficients. The absolute size of the node cannot explain the absence of the numerical retardation; the 80 node mesh in the MAGICO run produces a node 3.125 mm high while the 160 node mesh in the MIXA run produces a node 3.75 mm high. There are differences in the particle diameters, particle densities, and drop distances that probably determine whether or not the numerical retardation will appear. It is recommended that this type of 1-D analysis be performed with every calculation to determine if numerical retardation might be present.

It is important to note that the results of this numerical diffusion analysis are not directly

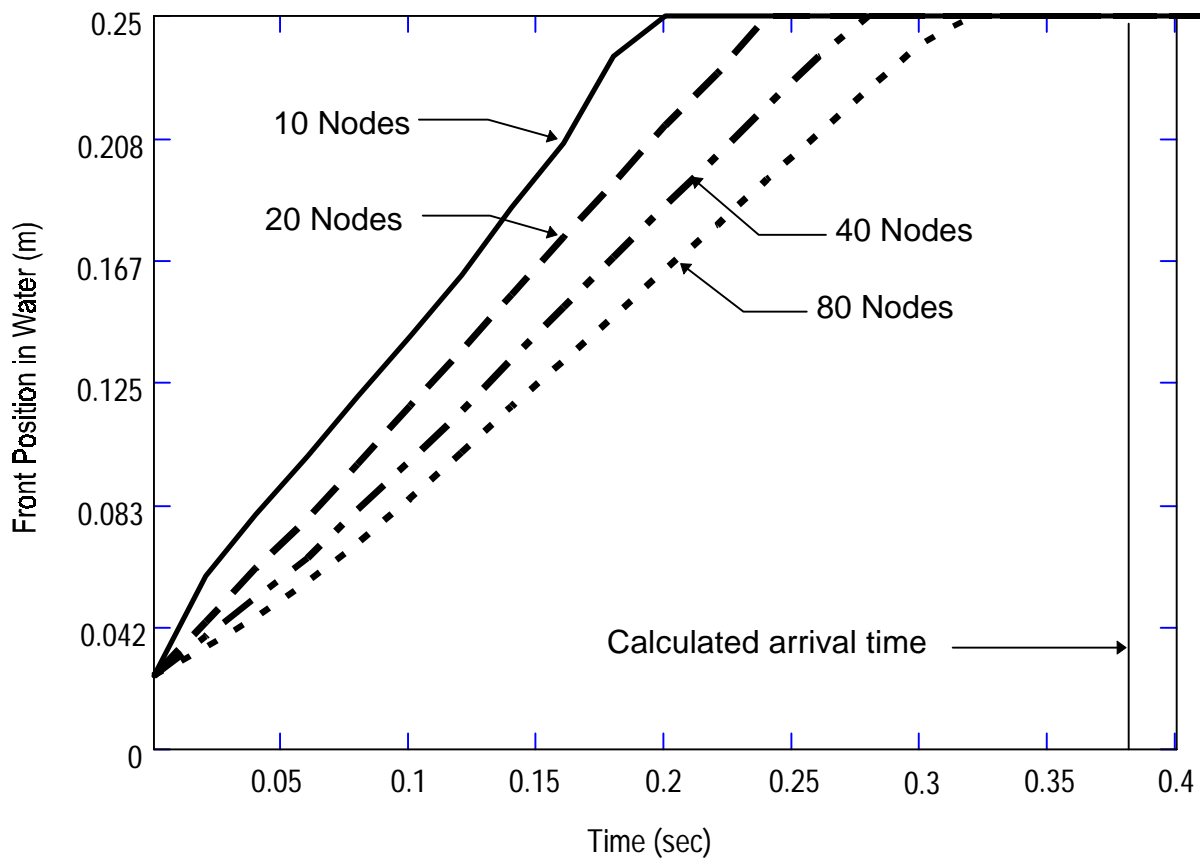


Figure 21 Effect of Mesh Refinement in MAGICO-701 on Numerical Diffusion

applicable to the two-phase boiling flows that are analyzed in the actual problem. There was some difference observed between the three MAGICO-701 meshes and little difference between the three MIXA-6 meshes. All of the calculations appear to produce front transit times that are shorter than those measured in the experiment. This may be due to numerical diffusion, in which case grid refinement may correct the problem. Another possibility is that the drag coefficients need to be modified. At this point in time, it is impossible to distinguish between the two alternatives. Procedurally, it is probably best to mesh the full problem as finely as possible under the current array sizes within IFCI (~1050 nodes). Results from this mesh should then be compared against the results from a coarser mesh. If the two runs substantially agree, then the problem solution is, of course, insensitive to mesh resolution differences between the two runs. If the runs differ substantially, then the results from the finer mesh are to be preferred, but the uncertainties associated with these differences cannot be fully resolved at this point. Thus further work to clarify this problem and make improvements would enhance the capabilities of IFCI.

Appendix B: Potential Impact of Pressurization in MIXA-6

When bubbles grow in a subcooled pool, the supplied energy is partitioned between vapor formation at the bubble surface and temperature elevation within the liquid. In the context of the coarse mixing stage of an FCI, this means that energy loss from the melt to a subcooled pool creates steam and a decrease in the subcooling of the water simultaneously. MIXA-6 was originally designed to be an isobaric experiment in which the saturation temperature was to remain constant. However, the steam generation rate was sufficiently high to create a modest pressurization from 0.1 MPa at the beginning of the experiment to about 0.13 MPa at 1 second. The difference in saturation temperatures at these two pressures (99.63 °C at 0.1 MPa and 107.13 °C, reference 17) is about 7.5 K. At first, it may seem like this is a minor perturbation that can be ignored. However, a closer examination of the global energy balance suggests that the pressurization cannot be ignored a priori.

One can determine whether subcooling can be ignored by comparing the energy of subcooling to the energy of the escaped steam. If the energy of subcooling is much less than the energy of the escaped steam, then subcooling can be ignored. Otherwise it cannot.

Based on a water specific heat of 4.187 kJ/kg-K and a water mass of 80 kg, there is a subcooling energy of about 2.5 MJ due to the increase in saturation temperature. The mass of steam generated by the experiment is obtained by integrating the product of the measured volume flow rate and the density as a function of saturation pressure. This integration produces a mass of 0.365 kg of steam that left the system between 0 and 1 second. Based upon an enthalpy of vaporization of 2.257 MJ/kg, the vaporization energy was 0.82 MJ. This is less than a third of the subcooling energy. If, instead, the subcooling energy were much smaller than the vaporization energy, the effect of pressurization could be ignored with confidence. Since the calculated subcooling energy is three times greater than the vaporization energy, the effects of subcooling cannot be ignored based on first principles.

Appendix C: Derivation of Inflow Boundary Conditions for MIXA-6

The published information [2] about the melt delivery in the MIXA-6 experiment is minimal. The paper indicates that 3 kg of melt was produced in the form of 6 mm droplets. The melt pour lasted approximately 1.5 seconds. The observed melt velocity at the water surface was initially ~5 m/seconds and it gradually decreased to 3.5 m/seconds over a period of about 0.2 seconds. With this information and some assumptions, a set of inflow conditions can be formulated.

In an effort to obtain better information about the process, Brian Turland of Winfrith was contacted. His description was more detailed and was used as the basis for this analysis. He wrote[18]:

It is believed that the pour lasted 1.5 s. Detailed measurements were made of the mass flux close to the initial water surface for the first 0.43 s. At this elevation the observed droplet speed was typically 3.8 m/s, and the mass flux, based on a central square area of 122 mm x 122 mm, was typically 130 kg/m²/s. During the later 1 s of the pour, obscuration prevented detailed measurement; for this period a velocity at the inflow location (melt release vessel) of 0.5 m/s was assumed and a mass flux of 140 kg/m²/s used. These figures give a total mass input of 3.06 kg (experimental value 3.00 kg). There is some uncertainty on these figures: higher mass fluxes are obtained earlier on if it is assumed that the flow tapers to zero rather than is constant in the later time-period.

The IFCI input deck requires a melt velocity and volume fraction for the inflow conditions. These were derived from the given information. First the fluxes were adjusted to reflect the cylindrical geometry used in the model. The diameter of the inflow boundary was specified as 120 mm (compared to the skirt diameter of 122 mm). By requiring that the melt fluence be the same, the mass fluxes become 171.08 kg/m²/second during the first 0.43 seconds, and 184.24 kg/m²/second for the remaining 1.07 seconds.

The flux at the inflow boundary (F_{inflow}) is related to the inflow velocity (V_{inflow}) and volume fraction (α_{inflow}) by the equation:

$$F_{inflow} = \rho_{melt} \alpha_{inflow} V_{inflow} , \quad (C-1)$$

where ρ_{melt} is the density of the melt. The velocity at the water surface (V_{entry}) is related to the inflow velocity by the integration of the acceleration equation:

$$V_{entry} = V_{inflow} + \sqrt{2 L g} , \quad (C-2)$$

where L is the free fall distance (1 m) and g is the gravitational constant. The entry velocity based upon zero inflow velocity is 4.4 m/sec, which is greater than the 3.8 m/second cited for the first 0.43 seconds of the pour. Since this part of the specification is not compatible with the free fall

calculation, it was decided to use an entry velocity of 5.0 m/second over the entire 1.5 seconds of the pour. This makes the inflow velocity 0.57131 m/second over the entire 1.5 seconds of the pour. The inflow volume fraction then becomes 0.03565 over the first 0.43 sec, and 0.038392 over the remaining 1.07 seconds.

Appendix D: Estimate of Thermal Radiation from Falling Melt to the Water

The measurements in the MIXA-6 experiment clearly indicate that steam is being forced through the flowmeter before the melt hits the water surface. While some of this might be due to convective and radiative heating of the existing steam by the melt, it is more likely that new steam is being generated by radiative heating of the water. This appendix presents a crude estimate of the steam generation rate due to radiative heating by the falling melt.

The droplet former creates a 4x4 grid of melt columns which break up into 6 mm droplets. In order to facilitate a simple calculation, the analysis will focus on the heat transfer from one of these columns of droplets. Droplets are created at the former with a period of τ . The former is at a distance L (1 m) from the water surface. They free fall in a column. The distance from water surface is denoted by the variable z .

The droplet formation period (τ) is calculated from the equation:

$$\tau = \frac{\frac{4}{3} \pi R_{drop}^3 \rho_{melt}}{\frac{1}{16} \frac{M}{\Delta t}} \quad (D-1)$$

where R_{drop} is the drop radius (3 mm), ρ_{melt} is the melt density (8400 kg/m³), M is the total mass delivered (3 kg), and Δt is the time interval over which that mass is delivered (1.5 sec). The calculated period is 7.602 milliseconds.

If an object begins falling at $t=0$ from the droplet former, its distance above the water surface is:

$$z(t) = L - V_{inflow} t - \frac{1}{2} g t^2 \quad (D-2)$$

where t is measured from initial melt release. The position of the first droplet is therefore $z(t-\tau)$, the second drop $z(t-2\tau)$, etc.

The heat transferred from the first drop (Q_{1st} , Watts, at temperature T_{drop}) to the surface of the water (at temperature T_{water}) is:

$$Q_{1st}(t) = A_{drop} \sigma (T_{drop}^4 - T_{water}^4) F_{d-p}(z(t-\tau)) H(t-\tau) \quad (D-3)$$

where $F_{d-p}(z)$ is the view factor between the drop and the water surface, and H is the Heaviside function. The view factor is a function of the distance between the drop center (z) and the water surface (radius, R_{pool} , of 0.21m), and is approximated by the formula for a concentrically aligned sphere and a disk [19]:

$$F_{d-p}(z) = \frac{1}{2} - \frac{1}{2 \sqrt{1 + \left(\frac{R_{pool}}{z} \right)^2}} \quad (D-4)$$

The heat transferred by the second drop is:

$$Q_{2nd}(t) = A_{drop} \sigma (T_{drop}^4 - T_{water}^4) \{F_{d-p}[z(t-2\tau)] - F_{d-d}[z(t-2\tau) - z(t-\tau)]\} H(t-2\tau) \quad (D-5)$$

Here, the view factor between the second drop and the water surface has been corrected for the inter-drop view factor, F_{d-d} , which is a function of the distance between the centers of the drops. If the blocking drop is approximated as a disk of the same radius, the inter-drop view factor becomes:

$$F_{d-d}(\Delta z) = \frac{1}{2} - \frac{1}{2 \sqrt{1 + \left(\frac{R_{drop}}{\Delta z} \right)^2}} \quad (D-6)$$

Similarly, the heat transferred by the third drop is:

$$Q_{3rd}(t) = A_{drop} \sigma (T_{drop}^4 - T_{water}^4) \{F_{d-p}[z(t-3\tau)] - F_{d-d}[z(t-3\tau) - z(t-2\tau)]\} H(t-3\tau) \quad (D-7)$$

Summing up the contributions from the drops in one column and multiplying by the number of columns (16) produces the heat transferred from the melt drops to the water surface (Q_{rad}).

$$Q_{rad}(t) = A_{drop} \sigma (T_{drop}^4 - T_{water}^4) \left[F_{d-p}(z(t-\tau)) H(t-\tau) + \sum_{n=2}^{N_{drop}(t)} \{F_{d-p}[z(t-n\tau)] - F_{d-d}[z(t-n\tau) - z(t-(n-1)\tau)]\} H(t-n\tau) \right] \quad (D-8)$$

This is converted into steam production by dividing by the water heat of vaporization (2257 kJ/kg) and multiplying by the change in specific volume ($1671.9 \times 10^3 \text{ m}^3/\text{kg}$). This steam production rate is plotted as a solid line in Figure 22 as a function of time after melt release. For reference, the experimentally measured rate of $0.25 \text{ m}^3/\text{second}$ is plotted as a dotted line. The calculated values range past $3 \text{ m}^3/\text{second}$ and show a dependence on melt front location that is not observed in the data (Figure 9). This is most likely due to the inter-column self-shielding between the droplets. This self-shielding should increase as the columns of melt get longer. A

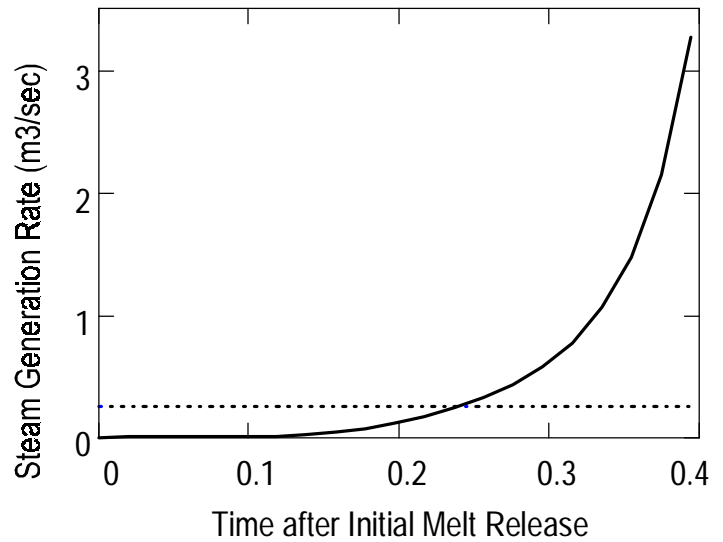


Figure 22 Calculated Steam Production Rate Due to Radiation from Falling Melt

more accurate calculation of steam production caused by the falling melt is beyond the scope of this analysis. This analysis does succeed in proving that radiation from the falling melt is the likely cause of the steam production that was measured before the entrance of the melt into the water.

Appendix E: Derivation of the Inflow Boundary for Krotos 38

Neither the Krotos-26 or 38 experiments were instrumented to monitor the inflow of molten alumina into the experiment cavity. This forces the modeler to make some approximation. The IFCI model of the Krotos-26 experiment started out with a solid column of melt suspended in the gas phase. This melt column then accelerated and fell into the water. This approximation has two disadvantages. First, the rate of melt entry into the water is likely to be unrealistically high. Second, a gas region equal in height to the column of melt must be meshed and included in the calculation.

The more desirable method of modeling melt entry into vessel is with an inflow condition. This requires values for the inflow volume fraction and velocity. An estimate for these values was obtained by a simple analysis of the melt delivery system.

In both the 26 and 38 experiments, the alumina was contained in a crucible and melted in a furnace which sat above the experiment cavity. When the alumina was raised to the desired temperature, the crucible was released and dropped down a pipe to the top of the jet. A “spike” on top of the tapered jet penetrated the bottom of the crucible, allowing the alumina to flow into the jet. This last phase is illustrated in Figure 23.

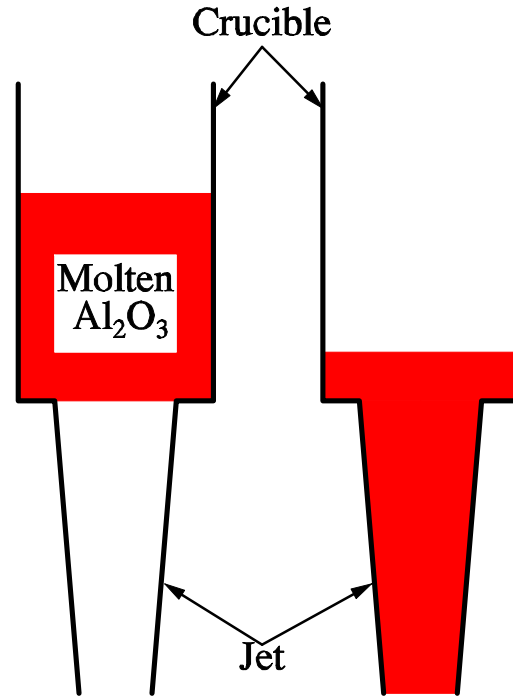


Figure 23 Schematic of the Crucible / Jet Configuration

The flow of the molten alumina into and out of the tapered jet was calculated based upon two approximations: 1) the flow was inviscid, and 2) the velocity was dominantly vertical and uniform at a single elevation. In the calculation, the change of the potential energy of the melt was equated to the sum of the kinetic energy of the melt and the time-integral of the momentum fluence out of the jet.

$$\rho_{melt} \int_{Crucible+Jet} A_c(z)[z(t=0) - z(t)] = \rho_{melt} \int_{Crucible+Jet} A_c(z) \frac{V_z^2}{2} + \rho_{melt} A_{exit} \int_0^t V_{exit} \frac{V_{exit}^2}{2} \quad (E-1)$$

This equation for mechanical energy is combined with the continuity equation and solved for the exit velocity (V_{exit}). The solution for the Krotos-38 experiment is shown in Figure 24. The calculated time for emptying the melt into the experiment cavity is approximately 0.46 seconds after the melt first starts to leave the jet. The average exit velocity is approximately 1.75 m/sec. The curve shown in Figure 24 was incorporated into the Krotos-38 input deck as an inflow

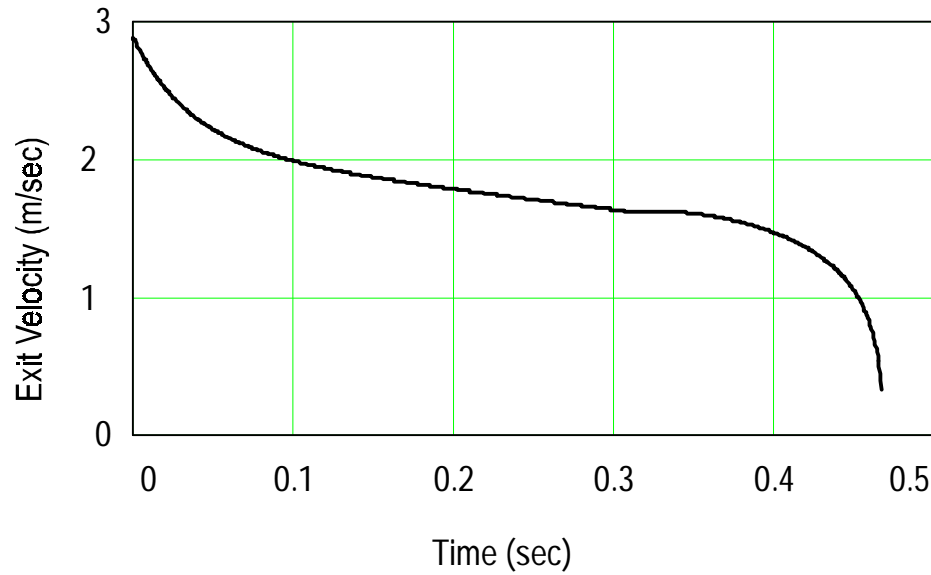


Figure 24 Computed Jet Exit Velocity as a Function of Time

condition. Since the width of the cell involved was the same as the jet diameter, the melt volume fraction for the inflow condition was set to unity.

Appendix F: Notes on Procedures

Users-Specified Input Parameters

The input deck for IFCI is composed of parameters that describe the physical dimensions of the experiment and those that control the numerical scheme. With the exception of the AL10 parameter, described in Appendix A, there was no attempt to optimize the numerical parameters. All of the numerical parameters used in the decks (Appendix G through K), with the exception of AL10 fall within the range recommended in the IFCI users manual.[16]

Meshing

Decisions about the meshing of a particular problem represent a compromise. The mesh must be fine enough to capture the physics being modeled and still fit into the computer memory and run in an acceptable amount of time. Appendix A showed that fine meshes are desirable to minimize numerical diffusion. Additionally, the numerical techniques used in IFCI work better if the length-to-width ratio of the cells is of the order of unity. Within IFCI itself, the total number of cells is limited to approximately 1050.

The initial mesh for the MAGICO-701 problem (pour radius: 10 cm, total radius: 20 cm, water height: 25 cm, total height: 40 cm) was a duplication of that used in the analysis performed by Angelini, et. al. [20]. They used 10 equally sized radial cells 2 cm in width and 16 vertical cells 2.5 cm in height. The mesh was refined in the axial direction because of concerns about numerical diffusion in the axial direction. There was no attempt to refine the mesh in the radial direction to examine radial numerical diffusion in this study. Axial refinements proceeded by factors of 2 to 32 and 64 axial cells. The final axial mesh of 104 cells was based upon the maximum number of cells that IFCI could handle. The vapor region was meshed as finely as the liquid region in these studies in order to try to capture the liquid swell, which was the quantity actually measured.

The rationale for the MIXA-6 (pour radius: 6 cm, total radius: 21 cm, water height: 60 cm, total height: 1.6 m) mesh was similar to, but not identical to that for the MAGICO mesh. The initial mesh of 11x36 nodes was created with the idea that modeling the mixing in the water was more important than modeling the convection in the gas. Therefore 16 axial cells (8 cells 6.0 cm long that model the vapor at the elevation of the skirt and 8 cells 6.5 cm long to model the vapor below the skirt) were used to model the vapor region and 20 axial cells of 3 cm length were used to model the liquid region. The pour radius was divided into 3 cells of 2 cm length to make the cells in the water approximately square. The remaining radial space (from 6 cm to 21 cm) was divided into 8 cells to keep the cell width approximately uniform. Refinements of this mesh were made only in the water region and only in the axial direction. Hence, the 11x56 mesh contained 40 axial cells in the water, and the 11x96 mesh contained 80 cells in the water. As in the MAGICO mesh, no attempt was made to examine radial numerical diffusion by refining the radial mesh.

Post-Processing

The FTN92 binary graphics output file was the data file processed in these analyses. The MPOST post-processing program was used to filter the desired output and write it out to an ASCII data file. The MPOST program and input instructions can be distributed as part of the IFCI package if requested.